Available online at www.sciencedirect.com
SCIENCE DIRECT®
Journal of Sound and Vibration 284 (2005) 51–73
JOURNAL OF SOUND AND VIBRATION
www.elsevier.com/locate/jsvi

Aerodynamic and aeroelastic analysis of bundled cables by numerical simulation

A.L. Braun, A.M. Awruch*

Civil Engineering, Federal University of Rio Grande do Sul, Av. Osvaldo Aranha, 99-3 Andar, Porto Alegre, RS CEP 90035-190, Brazil

Received 3 July 2003; accepted 5 June 2004
Available online 21 November 2004

Abstract

A numerical model for the aerodynamic and aeroelastic analysis of bundled cables, commonly used in energy transmission lines, is presented in this work. The bundles were idealized by a sectional model representing the section at the mid span between two supporting towers. A slightly compressible viscous fluid was considered and the two-dimensional flow was analyzed using a two-step explicit method with an arbitrary Eulerian–Lagrangean description. A Taylor series expansion was used in time and the classical Galerkin technique with the finite element method were used for space discretization. Turbulence was modeled using large eddy simulation with the classical Smagorinsky's sub-grid scale model. The set of cables forms a single body with elastic constrains working mechanically coupled, being each cable linked to the others by spacers. The fluid–structure interaction was taken into account considering equilibrium and compatibility conditions at the fluid–solid interfaces, and the resulting dynamical equilibrium equation was solved using the Newmark's method.

1. Introduction

Wind tunnel tests for assessment of aerodynamic and aeroelastic informations in the study of bundled cables performance are numerically simulated in this work. The usual way to obtain these

*Corresponding author. Tel.: +55 51 3316 3587; fax: +55 51 3316 3999.
E-mail address: awruch@adufrgs.ufrgs.br (A.M. Awruch).

0022-460X/$ - see front matter
doi:10.1016/j.jsv.2004.06.026

informations is using representative models in a wind tunnel. However, with the improvement in computer technology and computational fluid dynamics (CFD) algorithms, many of these problems can also be analyzed by numerical simulation.

Transmission lines are generally used to transport electrical energy through long distances. Initially, electrical energy was transported by a single conductor, but, in recent years, due to the growing demand, it was necessary to use several conductors grouped in bundles. Another reason that led to the employment of a set of cables in transmission lines with high electrical voltage was the need to reduce interferences in radio wave frequencies and to get improvements in transmission efficiency.

Bundled cables are formed by a group of parallel conductors separated at short distances by spacers, working mechanically coupled as a single body.

Although the determination of the aerodynamic coefficients of the set of conductors is necessary to estimate wind loads, studies about the dynamic stability of bundled cables is an essential aspect in order to get transmission lines with a satisfactory reliability. Galloping, a term suggested first by Den Hartog [1], is one of the most common dynamic instability phenomenon of bundled conductors, and its effect is characterized by a continuous growth of vibration amplitudes. This phenomenon appears suddenly, when the onset wind velocity is reached, resulting in a single-mode oscillatory motion perpendicular to the wind direction. Galloping may produce serious consequences, such as interruption in the energy supply and structural damages.

Several authors have studied the dynamic instability of bundled cables. Den Hartog [1] established the theoretical foundations of this problem. Wardlaw et al. [2] presented analytical and experimental results of the aeroelastic behavior of bundled conductors with different configurations; in this reference the analytical studies were based on the quasi-steady theory, and stability boundaries were determined for different cable layouts and compared with experimental values (obtained from sectional and 3-D models). The quasi-steady theory was also used by Price [3] to analyze flutter for a tandem arrangement of twin conductors. Tokoro et al. [4] presented a study about instability owing to galloping. They analyze the influence of horizontal distances between cables, angles of attack and structural damping using 3-D aeroelastic models. Nagao et al. [5] presented experimental results for a bundle formed by three conductors; they obtained the onset wind velocity which produces instability due to galloping for different angles of attack and Scruton numbers; the Scruton number is given by $Sc = 2m\delta/\rho D^2$, where m and D are the structural mass and the diameter of the cables, respectively, ρ is the fluid specific mass and δ is the logarithmic decrement.

Aerodynamic behavior of bundled cables has been also a subject matter of several researchers. Wardlaw [6] presents a detailed study about interference problems in bodies separated by short distances, determining aerodynamic coefficients for different angles of attack of the wind direction. Oliveira [7] presented experimental results for the drag and lift coefficients for bundles formed by two and four conductors as a function of the angle of wind incidence. Alam et al. [8] presented results of drag and pressure coefficients for a tandem arrangement with different distances between two parallel cables.

In this work, the analysis of the flow of a slightly compressible fluid in a two-dimensional domain was carried out using an explicit two-step Taylor–Galerkin method with an Arbitrary Lagrangean–Eulerian (ALE) description. A similar Taylor–Galerkin formulation was used by Tabarrok and Su [9] and by Rossa and Awruch [10], but with a semi-implicit scheme. The ALE

scheme was first presented by Hirt et al. [11] in a numerical work. Since this first paper, many authors used this description with the same concepts, such as Hughes et al. [12], Donea et al. [13], Liu et al. [14], Benson [15], among others. The classical Smagorinsky's model (see Murakami [16]) was employed for the sub-grid scales simulations in turbulent flows. The finite element method (FEM) was used for spatial discretization. The structure was considered as a rigid body with elastic restrains for the cross-section rotation and displacement components. The coupling between fluid and structure was performed applying the compatibility and equilibrium equations at the interface. The structural dynamic analysis was accomplished using the Newmark's method [17]. Examples are presented to illustrate the capability of the computational algorithm for aerodynamic and aeroelastic calculations.

2. Governing equations for the flow simulation

The governing equations for the fluid dynamic analysis are the well-known Navier–Stokes equations and the mass conservation equation [18]. In this work a slightly compressible turbulent flow and an isothermal process is considered. An ALE [19] description is considered, allowing the fluid–structure interaction analysis. Hence, the system of governing equations used here is given by:

(1) Momentum equations

$$\frac{\partial v_i}{\partial t} + (v_j - w_j)\frac{\partial v_i}{\partial x_j} + \frac{1}{\rho}\frac{\partial p}{\partial x_j}\delta_{ij} - \frac{\partial}{\partial x_j}\left[(\nu + \nu_t)\left(\frac{\partial v_j}{\partial x_i} + \frac{\partial v_i}{\partial x_j}\right) + \lambda\frac{\partial v_k}{\partial x_k}\delta_{ij}\right] = 0,$$
$$(i, j, k = 1, 2) \text{ in } \Omega. \tag{1}$$

(2) Mass conservation equation

$$\frac{\partial p}{\partial t} + (v_j - w_j)\frac{\partial p}{\partial x_j} + \rho c^2\frac{\partial v_j}{\partial x_j} = 0, \quad (j = 1, 2) \text{ in } \Omega. \tag{2}$$

In these equations, v_i and p (the velocity components and the pressure, respectively) are the unknown variables and ν_t is the eddy viscosity, characterizing a turbulent flow. The molecular viscosities $\nu = \mu/\rho$ and $\lambda = \chi/\rho$, the specific mass ρ and the sound speed c, are the fluid properties. The moving mesh velocity components are given by w_j, δ_{ij} is the Kroenecker delta and Ω is the domain to be analyzed.

The mass conservation equation, given by expression (2), was obtained considering the general equation of mass balance, which may be written as

$$\frac{\partial \rho}{\partial t} + v_j\frac{\partial \rho}{\partial x_j} + \rho\frac{\partial v_j}{\partial x_j} = 0, \quad (j = 1, 2) \text{ in } \Omega. \tag{3}$$

Taking into account that the velocity of sound propagation is given by $c^2 = \partial p/\partial\rho$, Eq. (3) may be expressed as

$$\frac{1}{c^2}\frac{\partial p}{\partial t} + \frac{v_j}{c^2}\frac{\partial p}{\partial x_j} + \rho\frac{\partial v_i}{\partial x_i} = 0. \tag{4}$$

Multiplying Eq. (4) by c^2 and considering an ALE description, Eq. (2) is obtained.

This form of the continuity equation corresponds to the so-called "pseudo-compressibility" hypothesis, introduced by Chorin [20] to solve incompressible flows. Slight compressibility is justified by natural flows, where the sound propagation has no infinite value (like in the air, for example), as predicted by the incompressibility assumption. This approach has been widely used by several authors to analyze incompressible flows, such as Kawahara and Hirano [21], He and Song [22], among others.

As a consequence of the extreme computational efforts necessary to simulate all the turbulence scales, large eddy simulation (LES) with Smagorinsky's sub-grid scale model [23] was employed. In this scheme the large scales are simulated directly and the small scales are simulated using a mathematical model. The governing equations for the large scales are obtained through a filtering process applied to Eqs. (1) and (2), where the variables (velocity components and pressure) are decomposed into two parts: large and sub-grid scale. Details of the filtering process may be found, for example, in Murakami [16]. After this filtering process, some unresolved terms arise; these terms are substituted by a turbulence closure model and the equations are finally expressed in terms of the large scale components. Each finite element in the mesh may be considered as a box filter, representing the cutting frequency in the Kolmogorov's energy dissipation curve. Hence, for high frequencies, related to the sub-grid scales, it is used as a model because the small elements are not able to represent these high frequencies. Smagorinsky [23] provided an expression, based on the Boussinesq's hypothesis, for the sub-grid terms, resulting in an eddy viscosity expression given by

$$\nu_t = (C_S \Delta)^2 (2 S_{ij} S_{ij})^{1/2}, \tag{5}$$

where S_{ij} is the strain rate tensor, C_S is the Smagorinsky's constant (taking values from 0.1 up to 0.25) and Δ is characteristic element (filter) dimension.

The boundary conditions of Eqs. (1) and (2) are

$$v_i = w_i \ \ (i = 1, 2) \text{ on the solid boundary } \ \Gamma_{v_s}, \tag{6}$$

$$v_i = \hat{v}_i \text{ on the boundary } \Gamma_{v_a} \text{ or } p = \hat{p} \text{ on the boundary } \Gamma_p, \tag{7}$$

$$\left[\frac{-p}{\rho}\delta_{ij} + (\nu + \nu_t)\left(\frac{\partial v_i}{\partial x_j} + \frac{\partial v_j}{\partial x_i}\right) + \lambda \frac{\partial v_k}{\partial x_k}\right] n_j = \frac{\sigma_{ij} n_j}{\rho} = S_i, \quad (i,j,k = 1,2) \text{ in } \Gamma_\sigma. \tag{8}$$

For a purely Eulerian description, the moving mesh velocity at each nodal point, with components w_i, is equal to zero. Now, for a purely Lagrangean description, the mesh motion velocity at each nodal point is equal to the fluid velocity, i.e. $v_i = w_i$ ($i = 1, 2$). Finally, in an Arbitrary Lagrangean–Eulerian formulation, the mesh velocity is not equal to zero and, at the same time, it is different of the fluid velocity at a specific point.

On the boundaries Γ_{v_a} and Γ_p, prescribed values for velocity and pressure, $\hat{v}_i$ and $\hat{p}$, respectively, must be specified, while on Γ_σ the boundary force components S_i must be in equilibrium with the stress tensor components σ_{ij}. In Eq. (8), n_j is the cosine of the angle formed by a vector perpendicular to Γ_σ and the axis x_j.

Initial conditions for the pressure and the velocity components at $t = 0$ must be given.

3. The algorithm for the flow simulation

Expanding the governing equations in Taylor series up to second order terms [24], the flow is analyzed with the following steps [25]:

(1) Calculate $\tilde{v}_i^{n+1/2}$ with

$$\tilde{v}_i^{n+1/2} = v_i^n + \frac{\Delta t}{2}\left\{-r_j\frac{\partial v_i}{\partial x_j} - \frac{1}{\rho}\frac{\partial p}{\partial x_j}\delta_{ij} + \frac{\partial}{\partial x_j}\left[\bar{\nu}\left(\frac{\partial v_i}{\partial x_j}+\frac{\partial v_j}{\partial x_i}\right) + \lambda\frac{\partial v_k}{\partial x_k}\delta_{ij}\right]^n + \left(\frac{\Delta t}{4}r_j r_k\right)\frac{\partial^2 v_i^n}{\partial x_j x_k}\right\}, \quad (9)$$

where $r_j = (v_j - w_j)$ and $\bar{\nu} = (\nu + \nu_t)$.

(2) Calculate $p^{n+1/2}$ with

$$p^{n+1/2} = p^n + \frac{\Delta t}{2}\left\{\left[-r_j\frac{\partial p}{\partial x_j} - \rho c^2\frac{\partial v_j}{\partial x_j}\right]^n + \left(\frac{\Delta t}{4}r_i r_j\right)\frac{\partial^2 p^n}{\partial x_j \partial x_i}\right\}. \quad (10)$$

(3) Calculate

$$\Delta p^{n+1/2} = p^{n+1/2} - p^n. \quad (11)$$

(4) Calculate $v_i^{n+1/2}$ with

$$v_i^{n+1/2} = \tilde{v}_i^{n+1/2} - \frac{1}{\rho}\frac{\Delta t^2}{8}\frac{\partial \Delta p^{n+1/2}}{\partial x_i}. \quad (12)$$

(5) Calculate $v_i^{n+1} = v_i^n + \Delta v_i$ with

$$\Delta v_i = \Delta t\left\{-r_j\frac{\partial v_i}{\partial x_j} - \frac{1}{\rho}\frac{\partial p}{\partial x_j}\delta_{ij} + \frac{\partial}{\partial x_j}\left[\bar{\nu}\left(\frac{\partial v_i}{\partial x_j}+\frac{\partial v_j}{\partial x_i}\right) + \lambda\frac{\partial v_k}{\partial x_k}\delta_{ij}\right]\right\}^{n+1/2}. \quad (13)$$

(6) Calculate $p^{n+1} = p^n + \Delta p$ with

$$\Delta p = \Delta t\left\{-r_j\frac{\partial p}{\partial x_j} - \rho c^2\left(\frac{\partial v_j}{\partial x_j}\right)\right\}^{n+1/2}. \quad (14)$$

These expressions must be employed after the classical Galerkin technique is applied into the FEM context. In this technique, the residual of the governing equations, where shape functions are used to approximate flow and geometric variables, are orthogonalized with respect to weight functions; in the Galerkin method, the same shape functions used to approximate geometric and flow variables are used as weight functions. A bilinear isoparametric quadrilateral element with four nodes was adopted in this work. More details about the FEM in fluid dynamics may be found in Reddy and Gartling [26], Gresho and Sany [27], among others.

As the scheme is explicit, the stability condition is given by

$$\Delta t_i < \beta\frac{\Delta x_i}{c + v_i}, \quad (i = 1, \ldots, NTE), \quad (15)$$

where $\beta < 1.0$ is a safety coefficient, Δx_i and v_i are the ith element characteristic dimension and the velocity, respectively, and NTE is the total number of elements.

Although a variable time step could be adopted [28], in this work a unique value of Δt was used, adopting the minimum value obtained with Eq. (15).

4. The fluid–structure coupling

In the present work, the structure is idealized as a two-dimensional rigid body. Displacement and rotations take place on the plane formed by the axis x_1 and x_2; the body is constrained by dampers and springs, as indicated in Fig. 1.

The structural dynamic equilibrium equation is given by the matricial expression

$$\mathbf{M}_S\ddot{\mathbf{U}}_S^c + \mathbf{C}_S\dot{\mathbf{U}}_S^c + \mathbf{K}_S\mathbf{U}_S^c = \mathbf{Q}_S^c, \tag{16}$$

where $\mathbf{M}_S$ is the mass matrix, $\mathbf{C}_S$ the damping matrix, $\mathbf{K}_S$ the stiffness matrix and $\ddot{\mathbf{U}}_S^c$, $\dot{\mathbf{U}}_S^c$ and $\mathbf{U}_S^c$ the acceleration, velocity and generalized displacements, respectively. Finally, $\mathbf{Q}_S^c$ is the load vector applied in the gravity center.

The subscript S means that these matrices belong to the structure and the superscript c indicates that these values correspond to the gravity center of the solid body. In Eq. (16), the dimension of all square matrices is 3×3, with non-zero elements only in the diagonal terms, while the dimension of the vectors is 3×1.

It must be noticed that the hypothesis considering a rigid structure is proper when deformations of the cross-section are small compared to the rotation and displacement components.

At the solid–fluid interface, the compatibility condition must be satisfied, or in other words, the fluid velocity and the structure velocity must be the same at the common nodes of both fields. The compatibility condition and the translation of variables evaluated at the gravity center of the body

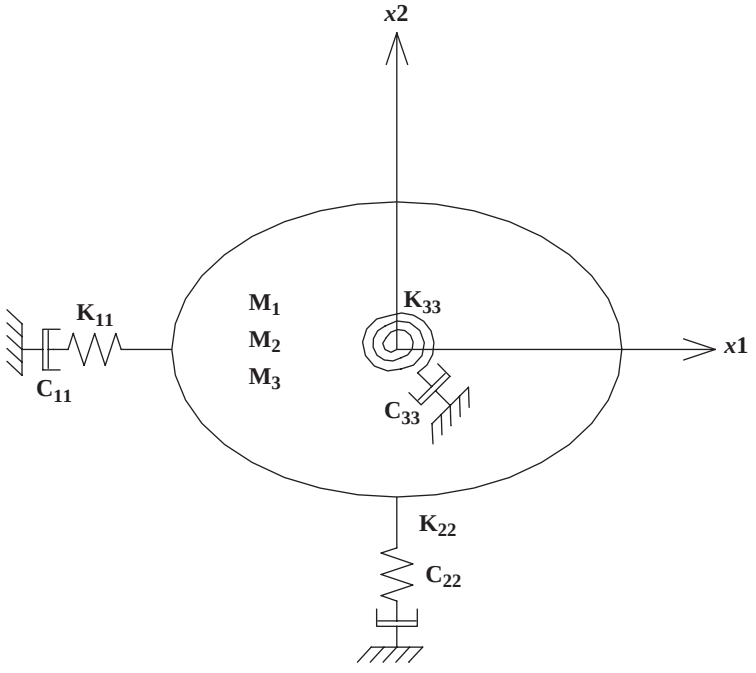

Fig. 1. Structure model, formed by a rigid body constrained by springs and dampers. Structure degrees of freedom: u_1 = displacement in the direction of axis x_1, u_2 = displacement in the direction of axis x_2, θ = rotation around the axis x_3 (perpendicular to the plane formed by the axes x_1 and x_2).

to a point located at the fluid–structure interface may be written with the following expressions:

$$\dot{\mathbf{U}}_S^I = \mathbf{V}_F^I = \mathbf{L}\dot{\mathbf{U}}_S^c \quad \text{with } \mathbf{L} = \begin{bmatrix} 1 & 0 & -l_2 \\ 0 & 1 & l_1 \end{bmatrix}, \tag{17}$$

where subscripts S and F are referred to the structure and the fluid, respectively, and the superscript I is referred to the interface. It is important to observe that both vectors, $\dot{\mathbf{U}}_S^I$ and $\mathbf{V}_F^I$, have two components that correspond to the global axis direction. However, $\dot{\mathbf{U}}_S^c$ has three components, because it includes the rotation around an axis perpendicular to the plane formed by x_1 and x_2. Values of $\dot{\mathbf{U}}_S^c$ can be transported to the solid–fluid interface (or to nodes belonging to the structure boundary) through a translation matrix $\mathbf{L}$, as given by Eq. (17), being l_1 and l_2 the distance components between the gravity center of the body and the point under consideration, measured in the global system. Considering Fig. 2, it is observed that the distance components from a boundary point to the body gravity center are functions of θ, and it may be written as

$$\mathbf{l}(\theta) = \begin{Bmatrix} l_1(\theta) \\ l_2(\theta) \end{Bmatrix} = \begin{bmatrix} \cos\theta & -\sin\theta \\ \sin\theta & \cos\theta \end{bmatrix} \begin{Bmatrix} x_{1g}^A \\ x_{2g}^A \end{Bmatrix} = \mathbf{R}\mathbf{x}_g^A. \tag{18}$$

Deriving Eq. (17) with respect to time, taking into account matrix $\mathbf{L}$ and Eq. (18), the following expression is obtained:

$$\ddot{\mathbf{U}}_S^I = \dot{\mathbf{V}}_F^I = \mathbf{L}\ddot{\mathbf{U}}_S^c + \mathbf{L}'(\dot{\theta})\dot{\mathbf{U}}_S^c, \quad \text{where } \mathbf{L}'(\dot{\theta}) = \begin{bmatrix} 0 & 0 & -l_1\dot{\theta} \\ 0 & 0 & -l_2\dot{\theta} \end{bmatrix}. \tag{19}$$

Eqs. (17) and (19) are applied to each node of the interface, where the equilibrium condition must also be satisfied, which means that the load $\mathbf{S}$ acting on the structure boundary, must be equal to the load $\mathbf{S}$ given by Eq. (8), but with an opposite sign (because here the fluid action on the structure is considered, while Eq. (8) represents the boundary action on the fluid). $\mathbf{S}$ can be

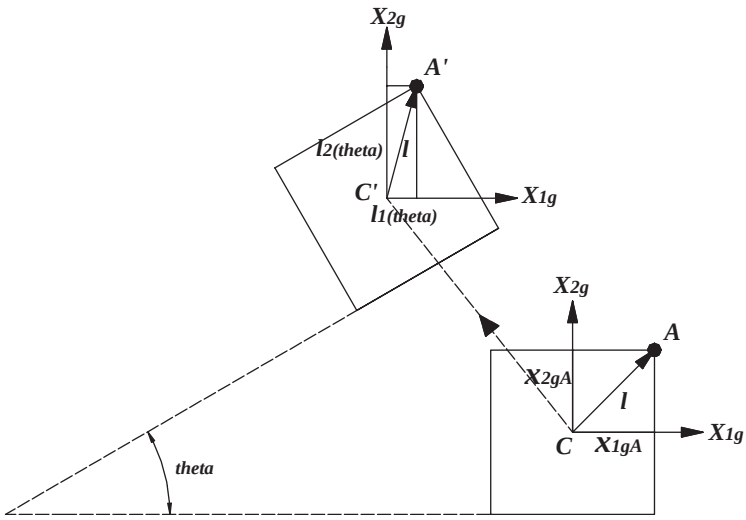

Fig. 2. Rigid body motion. The subscripts "g" and "l" are referred to quantities related to global and local axis, respectively.

transported to the gravity center of the body, and the force $\mathbf{Q}_S^c$, acting on the structure is given by

$$\mathbf{Q}_S^c = -\int_{\Gamma S} \mathbf{L}^{\mathrm{T}}\mathbf{S}\,\mathrm{d}\Gamma, \tag{20}$$

where $\mathbf{L}^{\mathrm{T}}$ is the transpose matrix of $\mathbf{L}$, given by Eq. (17), and $\mathbf{S}$ contains the two components of the fluid boundary force acting on the structure at a point located on the structure boundary Γ_S (Γ_S represents also the solid–fluid interface); the force components S_i, contained in vector $\mathbf{S}$, are given by Eq. (8), but with an opposite sign.

To determine the coupling effects between the fluid and the structure, in the FEM context, consider an element belonging to the fluid domain in contact with the solid body, as indicated in Fig. 3, where it can be observed that only points 1 and 2 are in contact with the structure.

The momentum equations in its matricial form, at element level (e), can be obtained by applying the Galerkin method to Eq. (1).

Regarding the structural analysis, the matricial expression that contributes to the assembling of the overall dynamic equilibrium equation is

$$\mathbf{MM}^{II}\dot{\mathbf{V}}^I + \mathbf{AD}^{II}\mathbf{V}^I + \mathbf{MM}^{IF}\dot{\mathbf{V}}^F + \mathbf{AD}^{IF}\mathbf{V}^F - \frac{1}{\rho}\mathbf{GP}^I = \mathbf{S}^I. \tag{21}$$

In Eq. (21), $\dot{\mathbf{V}}^I$ and $\mathbf{V}^I$ contain, respectively, acceleration and velocity components corresponding to nodes 1 and 2 of Fig. 3, while $\dot{\mathbf{V}}^F$ and $\mathbf{V}^F$ contain variables corresponding to nodes 3 and 4 of the same figure. A similar remark can be made with respect to the vectors of

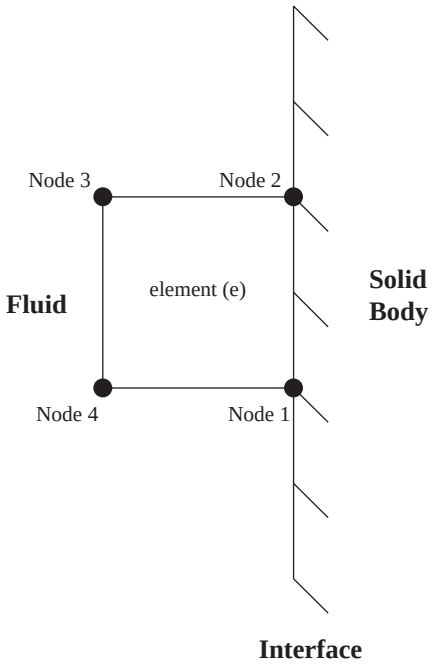

Fig. 3. Element of the fluid domain, in contact with the solid body.

pressure gradients **GP** and boundary forces **S**. Matrix $\mathbf{MM}^{II}$ contains elements coming from the connection of node 1 with node 2. Matrix $\mathbf{MM}^{IF}$ contains elements originated by the connection between the nodes 1 with 4 and 2 with 3. Similar commentaries can be made with respect to matrices $\mathbf{AD}^{II}$ and $\mathbf{AD}^{IF}$.

Eq. (17) with matrix **L** and Eq. (19) with matrix $\mathbf{L}'(\dot{\theta})$ are considered for each node at the interface. Then, when an element side with its two nodes lying on the fluid–structure interface is considered, Eq. (17) and (19) are written in the form

$$\dot{\mathbf{U}}_S^I = \mathbf{V}^I = \mathbf{T}\dot{\mathbf{U}}_S^c, \quad \ddot{\mathbf{U}}_S^I = \dot{\mathbf{V}}^I = \mathbf{T}\ddot{\mathbf{U}}_S^c + \mathbf{T}'(\dot{\theta})\dot{\mathbf{U}}_S^c. \tag{22}$$

Referring again to Fig. 3, the matrices **T** and $\mathbf{T}'$ are given by

$$\mathbf{T} = \left[\begin{array}{ccc} 1 & 0 & -l_2^1 \\ 0 & 1 & l_1^1 \\ \hline 1 & 0 & -l_2^2 \\ 0 & 1 & l_1^2 \end{array}\right] = \left[\begin{array}{c} \mathbf{L} \\ \hline \mathbf{L} \end{array}\right], \quad \mathbf{T}'(\dot{\theta}) = \left[\begin{array}{ccc} 0 & 0 & -l_1^1 \\ 0 & 0 & -l_2^1 \\ \hline 0 & 0 & -l_1^2 \\ 0 & 0 & -l_2^2 \end{array}\right]\dot{\theta} = \left[\begin{array}{c} \mathbf{L}'(\dot{\theta}) \\ \hline \mathbf{L}'(\dot{\theta}) \end{array}\right], \tag{23}$$

where the superscript i (= 1, 2) indicates the local node number at the interface and the subscript j (= 1, 2) indicates the component in the direction of the axis x_j.

The contribution from $\mathbf{S}^I$, on the side 1–2 of the element (e), to the total load acting at the gravity center of the body, can be calculated with the expression

$$\hat{Q}_S^c = -\mathbf{T}^{\mathrm{T}}\mathbf{S}^I. \tag{24}$$

Considering Eqs. (16), (17), (19) and (21), with the last one multiplied by ρ, the structural dynamic equilibrium equation, taking into account the solid–fluid coupling effect, is given by

$$\left[\mathbf{M}_S + \sum_{i=1}^{NTL}(\mathbf{T}^{\mathrm{T}}\rho\mathbf{MM}^{II}\mathbf{T})_i\right]\ddot{\mathbf{U}}_S^c + \left[\mathbf{C}_S + \sum_{i=1}^{NTL}(\mathbf{T}^{\mathrm{T}}\rho\mathbf{AD}^{II}\mathbf{T} + \mathbf{T}^{\mathrm{T}}\rho\mathbf{MM}^{II}\mathbf{T}')_i\right]\dot{\mathbf{U}}_S^c + \mathbf{K}_S\mathbf{U}_S^c$$
$$= -\left[\sum_{i=1}^{NTL}(\mathbf{T}^{\mathrm{T}}\rho\mathbf{MM}^{IF}\dot{\mathbf{V}}^F + \mathbf{T}^{\mathrm{T}}\rho\mathbf{AD}^{IF}\mathbf{V}^F - \mathbf{T}^{\mathrm{T}}\mathbf{GP}^I)_i + \mathbf{Q}_S^c\right], \tag{25}$$

where NTL is the total number of fluid elements in contact with the structure, having at least one straight segment common to the solid body boundary, forming the solid–fluid interface. The matricial Eq. (25) may be re-written in a compact form as

$$\overline{\mathbf{M}}_S\ddot{\mathbf{U}}_S^c + \overline{\mathbf{C}}_S\dot{\mathbf{U}}_S^c + \mathbf{K}_S\mathbf{U}_S^c = \overline{\mathbf{Q}}_S^c. \tag{26}$$

It can be noticed that $\overline{\mathbf{C}}_S$ is a nonlinear and a non-symmetric matrix, because it contains the advective terms and $\left[\mathbf{T}^{\mathrm{T}}\mathbf{MM}^{II}\mathbf{T}'(\dot{\theta})\right]$.

The analysis for both fields is made in a sequential way. First, Eqs. (9)–(14) are solved, with the smallest Δt calculated with Eq. (15) and applying the boundary conditions given by Eqs. (6)–(8). After this, Eq. (26) is solved using the Newmark's method [17].

5. Aerodynamic coefficients calculation and automatic mesh motion scheme

The drag coefficient C_D is related to the forces acting on the structure in the direction X_{1g}, according to Fig. 2, while the lift coefficient C_L is related to the forces acting on the structure in the direction X_{2g}, regarding the same figure referred above. On the other hand, the Strouhal number (St) is a non-dimensional number referred to the vortex shedding phenomenon observed in immersed bodies. These three coefficients are obtained from the equations

$$C_D = \frac{\sum_{i=1}^{NTN} S_{1i}^I}{\frac{1}{2}\rho V_0^2 L_0}, \quad C_L = \frac{\sum_{i=1}^{NTN} S_{2i}^I}{\frac{1}{2}\rho V_0^2 L_0}, \quad St = \frac{f_v L_0}{V_0}, \tag{27}$$

where ρ is the fluid specific mass, V_0 is a characteristic velocity (the inflow velocity), L_0 is a characteristic dimension of the body (the cylinder diameter D), f_v the shedding frequency (obtained from the curve describing variations of the lift coefficient in time) and S_1^I and S_2^I are the forces in the directions of the axis x_1 and x_2, respectively, acting on the structure at node i, located on the interface. NTN is the total number of nodes located on the solid–fluid interface. The forces S_1^I and S_2^I are the components of the force vector $\mathbf{S}^I$, given by Eq. (21). These forces are applied to the structure on each fluid element side belonging to the interface.

Force components S_1^I and S_2^I are obtained by the finite element discretization of Eq. (8) over the fluid–structure interface, considering a trapezoidal distribution of the fluid load in both directions. The effects of the fluid on the immersed body is given by

$$\begin{aligned}\mathbf{S}_j^I = \begin{Bmatrix} S_j^1 \\ S_j^2 \end{Bmatrix} &= \int_{l_{1-2}} \begin{Bmatrix} \Phi_1 \\ \Phi_2 \end{Bmatrix} (\Phi_1 S_j^1 + \Phi_2 S_j^2)\mathrm{d}l = \int_{l_{1-2}} \begin{bmatrix} \Phi_1^2 & \Phi_1\Phi_2 \\ \Phi_2\Phi_1 & \Phi_2^2 \end{bmatrix} \begin{Bmatrix} S_j^1 \\ S_j^2 \end{Bmatrix} \mathrm{d}l \\ &= \int_{-1}^{1} \begin{bmatrix} (1-\xi)^2 & (1+\xi)(1-\xi) \\ (1+\xi)(1-\xi) & (1-\xi)^2 \end{bmatrix} \begin{Bmatrix} S_j^1 \\ S_j^2 \end{Bmatrix} \frac{l_{1-2}}{8}\mathrm{d}\xi = \frac{l_{1-2}}{6} \begin{Bmatrix} 2S_j^1 + S_j^2 \\ S_j^1 + 2S_j^2 \end{Bmatrix}, \quad (j = 1, 2)\end{aligned} \tag{28}$$

where l_{1-2} represents an interface segment length, j indicates the force component in the direction of the axis x_j, ξ is the natural coordinate of the integration domain, Φ_1 and Φ_2 are the interpolation functions and 1 and 2 are the local node numbers of the fluid element belonging to the body boundary.

Taking into account that the immersed body in the fluid can move and rotate in its plane and that the flow is described by an arbitrary Lagrangean–Eulerian (ALE) formulation, a scheme for the mesh motion is necessary, establishing the velocity field $\mathbf{w}$ in the fluid domain, such that the element distortion will be as smaller as possible, according to the following boundary conditions:

$$\mathbf{w}_{\text{interface}} = \mathbf{V}_F^I = \dot{\mathbf{U}}_E^I, \quad \mathbf{w}|_{\text{external boundaries}} = 0. \tag{29}$$

In the present work, the mesh motion scheme is similar to that used by Teixeira and Awruch [29]. Considering that i is an inner node in the fluid field and j is a boundary node, the mesh

velocity components at node i, in the direction of the axis x_k, are given by

$$w_k^i = \frac{\sum_{j=1}^{NS} a_{ij} w_k^j}{\sum_{j=1}^{NS} a_{ij}}, \quad (k = 1, 2), \tag{30}$$

where NS is the total number of nodes belonging to the boundary lines and a_{ij} are influence coefficients between inner nodes and nodes belonging to the boundaries of the flow field, being $a_{ij} = 1/(d_{ij})^n$, where d_{ij} is the distance between i and j, and $n \geqslant 1$. The exponent n can be adjusted by the user.

6. Numerical applications

6.1. Aerodynamic analysis of bundled cables

In this numerical application, drag and lift coefficients for some characteristic bundle layouts were determined. As depicted in Fig. 4, three different studies were carried out. First, in a wake interference study (case (a)), forces on a smooth circular cylinder behind an identical upstream cylinder at a fixed horizontal distance ($X/D = 10$) were obtained as a function of the cross-stream position (Y/D). Finally, the wind forces as functions of the flow incidence angle on two typical cable configurations employed in power lines were estimated (cases (b) and (c)). In the last two cases, the forces are measured at the bundle mechanical center, taking into account the contribution of all cables, as indicated in Fig. 4.

Geometrical and fluid flow characteristics used in the numerical simulations are given in Table 1. The time intervals adopted in the present work were $\Delta t = 5 \times 10^{-5}$, 2×10^{-5} and 3×10^{-5} s, for the configurations (a), (b) and (c) in Fig. 4, respectively. All simulations were carried out using 1.5×10^6 time steps and values of the mean forces were calculated considering the last 5×10^5 time increments. The non-slip boundary condition was prescribed on the body surfaces.

The finite element meshes for the three cases were built using quadrilateral bilinear isoparametric elements and regions such as boundary layers and wake areas were carefully refined in order to get similar results to those obtained with experimental works. The smallest element dimension observed in the finite element meshes was about $10^{-3} \times D$.

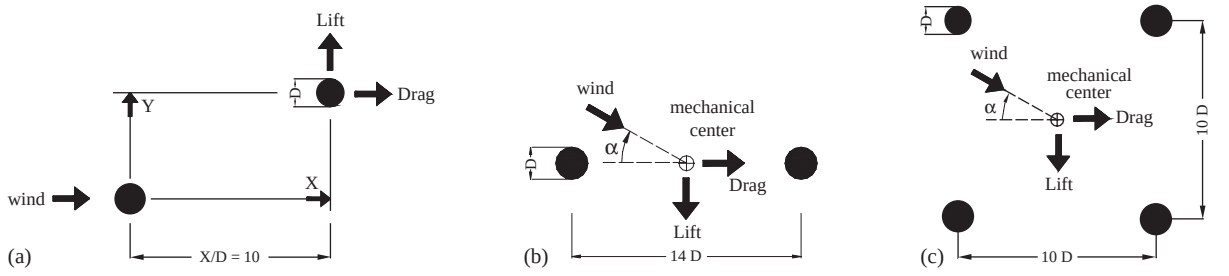

Fig. 4. Configurations of the cables employed in the aerodynamic analysis: (a) cable in downstream position in a wake interference study; (b) bundle with two cables; and (c) bundle with four cables.

Table 1
Fluid properties according to the cables set configuration

Aerodynamic analysis–fluid constants	
Downstream cable of a twin set	
Specific mass (ρ) (kg/m^3)	1.2
Kinematic viscosity (v)(m^2/s)	3.85×10^{-4}
Reynolds number (Re)	2.6×10^4
Mach number ($M = V_0/c$) (c=sound vel.)	0.030
Reference velocity (V_0) (m/s)	10.0
Smagorinsky′s constant (C_S)	0.2
Characteristic dimension (L_0) (m)	1.0
Bundle with two cables	
Specific mass (ρ) (kg/m^3)	1.2
Kinematic viscosity (v) (m^2/s)	4.13×10^{-7}
Reynolds number (Re)	3×10^4
Mach number ($M = V_0/c$) (c=sound vel.)	0.052
Reference velocity (V_0) (m/s)	0.5
Smagorinsky's constant (C_S)	0.2
Characteristic dimension (L_0) (m)	0.0248
Bundle with four cables	
Specific mass (ρ) (kg/m^3)	1.2
Kinematic viscosity (v) (m^2/s)	3.10×10^{-7}
Reynolds number (Re)	4×10^4
Mach number ($M = V_0/c$) (c=sound vel.)	0.068
Reference velocity (V_0)(m/s)	0.5
Smagorinsky's constant (C_S)	0.2
Characteristic dimension (L_0) (m)	0.0248

Wake interference studies in terms of force coefficients (drag and lift forces) are shown in Fig. 5, where a comparison with the experimental work carried out by Wardlaw and Cooper [30] (also published in Ref. [6]) is also presented. Results for drag and lift coefficients for the two bundles with different flow incidence angles are shown in Fig. 6, where comparison with an experimental model performed by Oliveira [7] is also presented.

Strouhal numbers were computed for the different cases presented in this section and they are summarized in Table 2, where comparisons with experimental data for a single cylinder obtained from Schlichting [18] are shown. It can be noticed that there is no significant differences between each case studied here and the single cylinder. An exception is the four-bundle arrangement, where a higher shedding frequency (f_v) is verified.

Instantaneous streamlines and pressure fields for the wake interference analysis corresponding to the different cross-stream positions are presented in Fig. 7. The same fields corresponding to the two bundles and for the different angles of attack are shown in Fig. 8.

The drag and lift force profiles in Figs. 5 and 6 are clearly consistent with the fields presented in Figs. 7 and 8. The lift force increases from $Y/D = 0$, where the symmetry reproduces the single

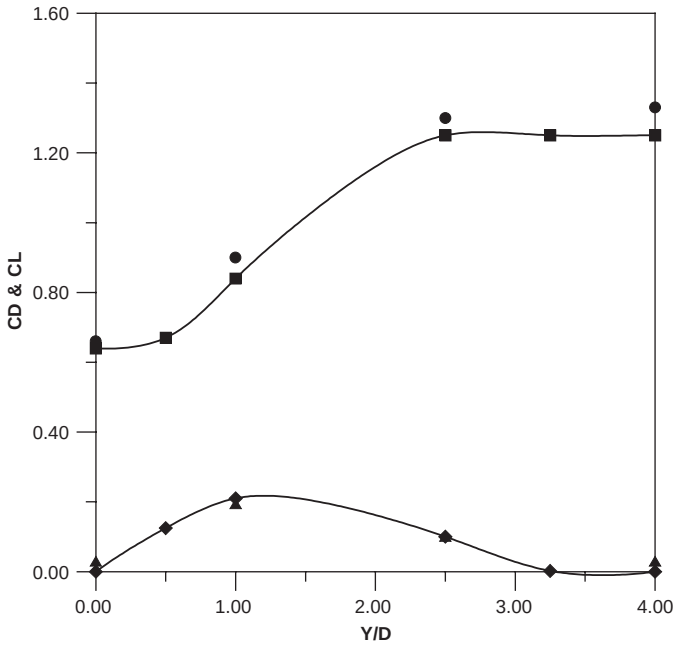

Fig. 5. Aerodynamic coefficients obtained in the wake interference analysis. Drag coefficient C_D: (●) present work; (■) Wardlaw and Cooper [30]. Lift coefficient C_L: (▲) present work; (◆) Wardlaw and Cooper [30].

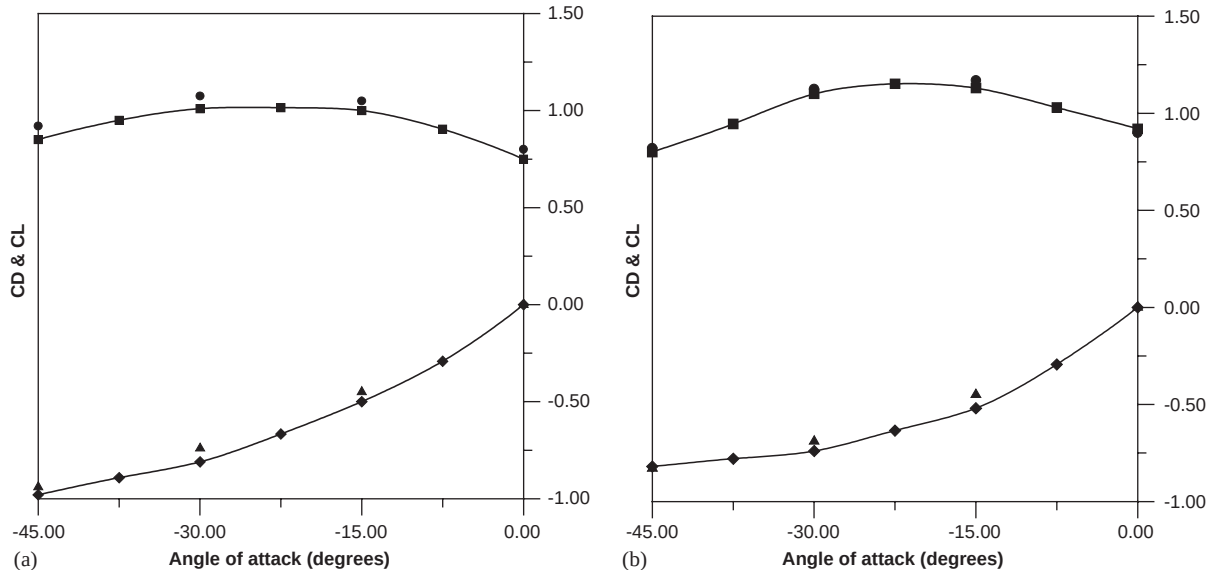

Fig. 6. Aerodynamic coefficients obtained in the bundled cables analysis: (a) bundle with two cables; (b) bundle with four cables. Drag coefficient C_D: (●) present work; (■) Oliveira [7]. Lift coefficient C_L: (▲) present work; (◆) Oliveira [7].

Table 2
Strouhal number computed according to the cables set arrangement

Cables set arrangements	Angle of attack (α)				Cross-stream position (Y/D)			
	0°	15°	30°	45°	0	1	2.5	4
Bundle with two cables	0.220	0.184	0.191	0.212	—			
Bundle with four cables	0.227	0.222	0.233	0.210				
Downstream cable of a twin set	—				0.160	0.167	0.185	0.195
Single cylinder [18]					0.190			

cylinder situation, until $Y/D \approx 1$ where wake effects are more intensive. Then, the lift force begins to decrease owing to the reduction of wake interference as the relation Y/D increases. The drag force has its smallest value when $Y/D = 0$, due to the wake turbulence, causing the transition at a lower Reynolds number. As the separation between the cylinders (given by the relation Y/D) increases, the drag force converges to the value of the single cylinder.

The same commentaries can be applied to the bundles, but now forces are functions of the incidence angle. The lift force has inexpressive values for small incidence angles due to the cables symmetry when they are referenced to the stream direction. As the wind angle of attack increases the bundle cross section becomes asymmetric and consequently the lift force becomes larger. On the other hand, the drag force values are directly related to the area of the cables set exposed to the fluid stream. For a flow incidence angle equal to zero, the wake turbulence produced by the bundle upstream components generates a reduction of the global drag. For incidence angles ranging from 15° to 30°, practically the total area of the cables set is exposed to the fluid stream and higher values of the drag force are obtained. For incidence angles ranging from 30° to 45° a gradual reduction of the global drag is observed, when the bundle downstream components are immersed in the wake of the upstream components again, similarly to the case where the angle of attack is equal to zero.

An important factor, which may cause some differences between numerical and experimental results, is the cables roughness when the cable bundles are analyzed; while the experimental model was carried out with rough cables, the numerical simulation did not take into account this characteristic of the cables surfaces. In spite of these reasons, good agreements were obtained between numerical and experimental simulations, once the adopted Reynolds number belongs to the sub-critical region where the cables roughness does not influence the results when compared to cables with smooth surfaces.

6.2. Dynamic instability due to galloping

Analysis of dynamic instability owing to galloping in a set of two and three aligned and coupled cables is presented in this section. The main objective is to reproduce aeroelastic tests, where the cables motion interacts with the surrounding fluid motion. As it was previously mentioned, galloping is characterized by structural vibrations of large amplitude in the perpendicular

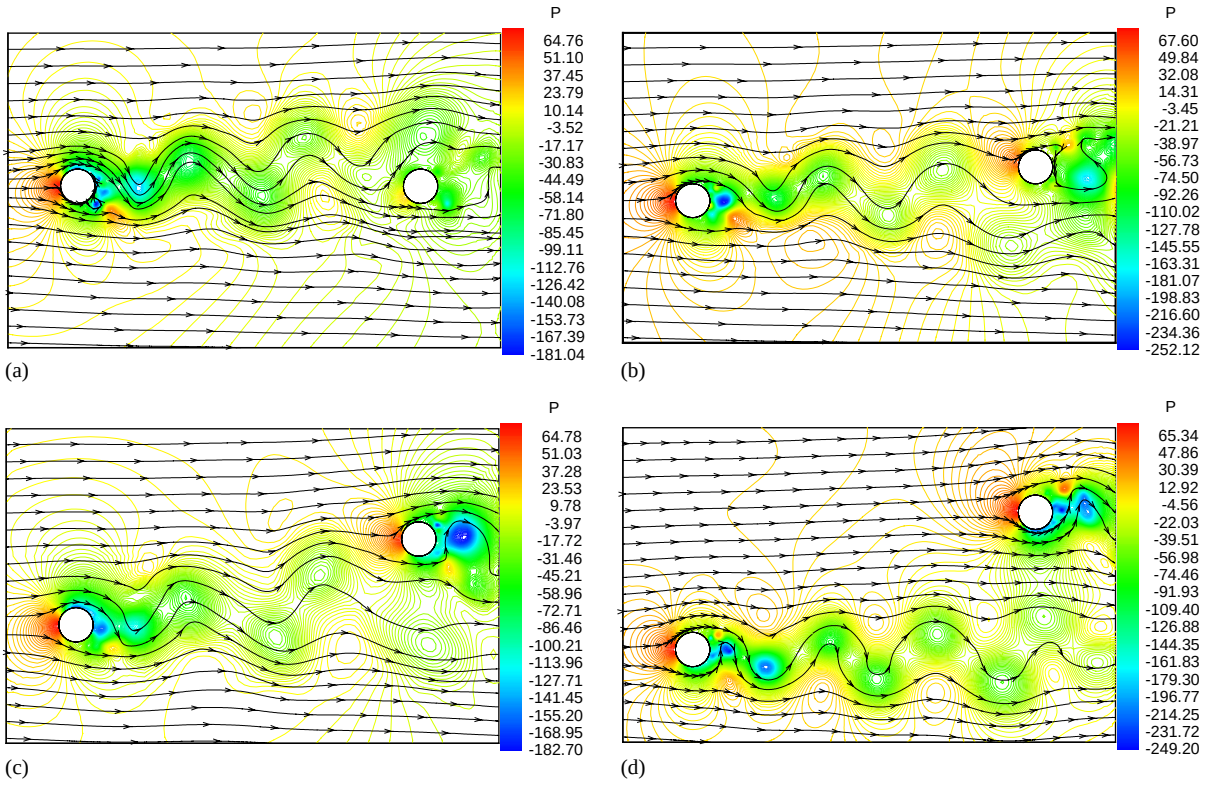

Fig. 7. Instantaneous streamlines and pressure fields obtained in the wake interference analysis. (a) $Y/D=0$; (b) $Y/D=1$; (c) $Y/D=2.5$; (d) $Y/D=4$.

direction to the flow. The critical wind velocity or onset wind velocity is identified when the structure begins to show oscillating displacements with large magnitude. The numerical simulation aims to reproduce some of the experimental tests carried out by Tokoro et al. [4] and Nagao et al. [5] for wake galloping situations.

The first application was performed in order to study the wake-galloping phenomenon for a leeward cable of a twin cable arrangement (see Fig. 9). Results of this numerical analysis were compared with those obtained with an experimental work by Tokoro et al. [4] for a specific aerodynamic and structural condition. The cable arrangement was submitted to a wind with an incidence angle equal to 15° and the structural response was a consequence of the forces acting on the mechanical center of the downstream cylinder considering that the upstream cylinder was fixed.

The second application was based on the experimental work developed by Nagao et al. [5], where a set formed by three bundled cables separated by the same distance and with the same diameter (see Fig. 10) was analyzed. Mechanically, the structure was represented by the mid span section, which has three degrees of freedom: two displacements components and a rotation representing the bundle torsion. The adopted angle of wind incidence was 17°.

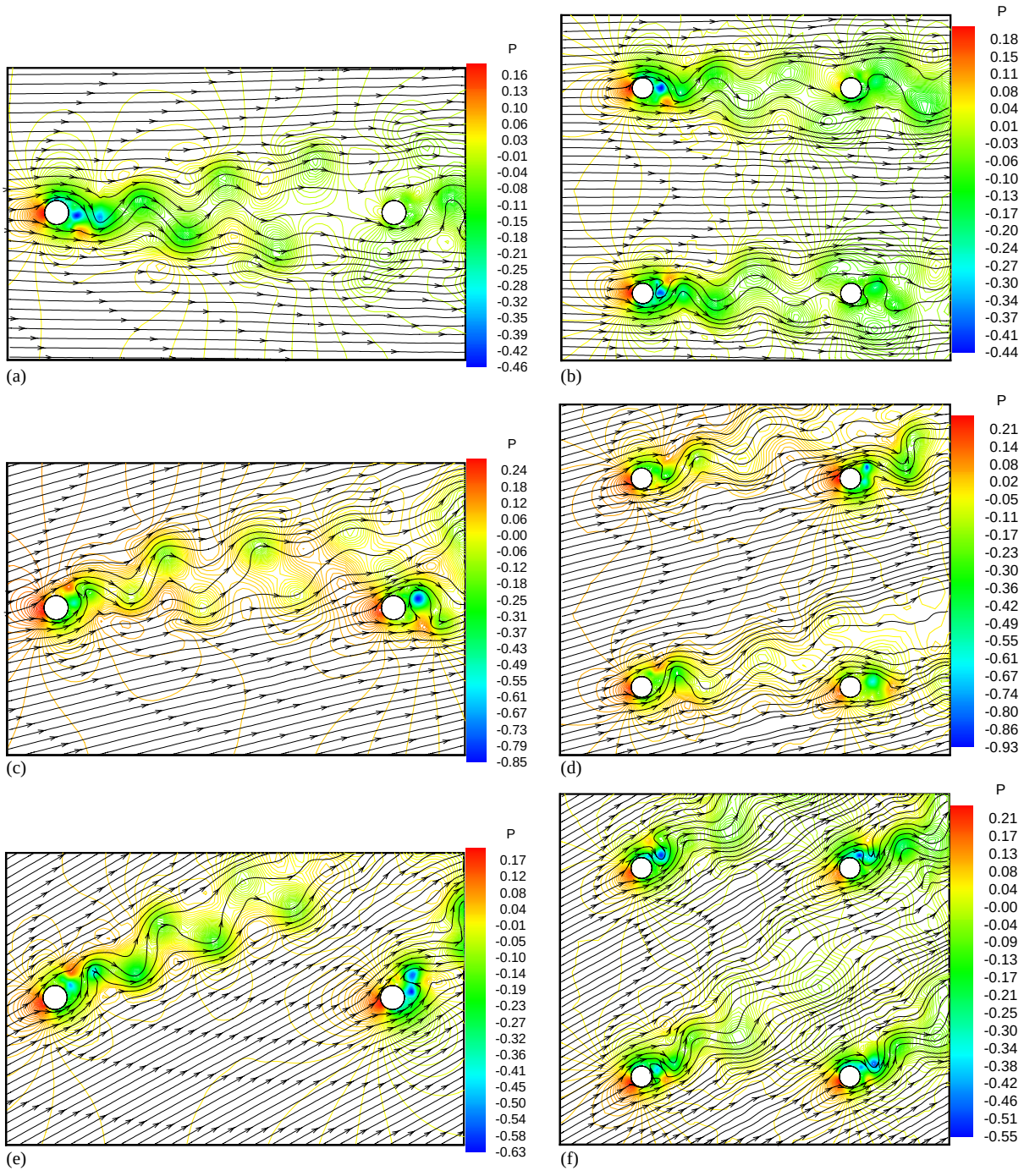

Fig. 8. Instantaneous streamlines and pressure fields obtained in the bundled cables analysis. $\alpha = 0^{\circ}$: (a) bundle with two cables and (b) bundle with four cables. $\alpha = 15^{\circ}$: (c) bundle with two cables and (d) bundle with four cables. $\alpha = 30^{\circ}$: (e) bundle with two cables and (f) bundle with four cables. $\alpha = 45^{\circ}$: (g) bundle with two cables and (h) bundle with four cables.

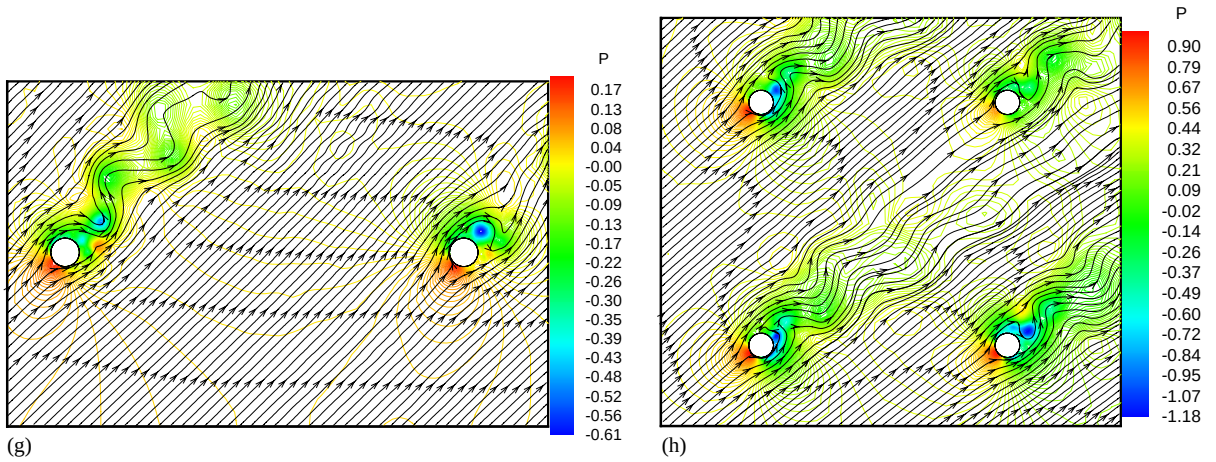

Fig. 8. (*Continued*)

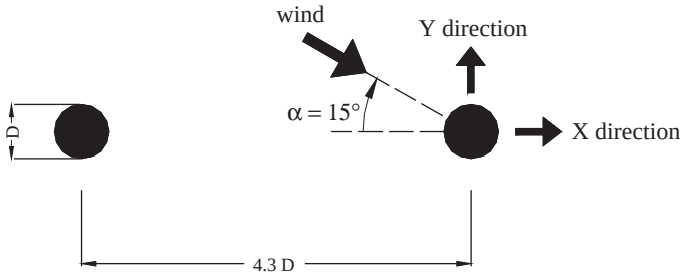

Fig. 9. Geometrical characteristics of the wake galloping analysis for a cable in the leeward position of a twin cable arrangement.

Fluid properties as well as the geometrical characteristics are presented in Table 3. Reynolds numbers (with the cable diameter as characteristic length) ranging from 2.4×10^4 to 1.15×10^5 were adopted. For both applications an oblique flow was imposed prescribing the inflow velocity components in the global coordinate directions on the external boundaries (excepting the outflow boundary, where boundary forces were considered). Compatability and equilibrium boundary conditions were prescribed on the body surfaces.

The time intervals adopted for the time marching process were $\Delta t = 2 \times 10^{-5}$ s and $\Delta t = 1.15 \times 10^{-5}$ s for the first and the second applications, respectively.

The main structural properties are presented in Table 4. It is important to notice that the same natural frequencies, damping ratio and inertia are considered for all the vibration modes in the case of the three bundled cables, as in the experimental model. Structural damping was obtained from the Scruton number, taking into account that $Sc = 2m\delta/\rho D^2 \cong 4\pi m\xi/\rho D^2$ (where it was considered that the logarithmic decrement δ is approximately equal to $2\pi\xi$, with ξ being the

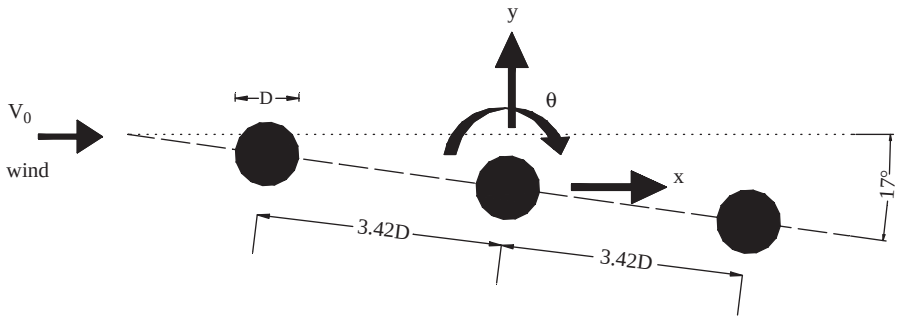

Fig. 10. Geometrical characteristics of the galloping analysis for a set of three cables in bundle arrangement.

Table 3
Fluid properties according to cables set arrangement (aeroelastic analysis–fluid constants)

Fluid properties (three bundled cables)	Fluid velocities (m/s)			
	9.0	9.6	12.0	
Reynolds number (Re)	2.40×10^4	2.56×10^4	3.20×10^4	
Mach number ($M = V_0/c$) (c=sound vel.)	0.027	0.029	0.036	
Kinematic viscosity (v) (m^2/s)		1.5×10^{-5}		
Smagorinsky's constant (C_S)		0.12		
Characteristic dimension (L_0) (m)		0.04		
Fluid properties (leeward cable of a twin arrangement)	Fluid velocities (m/s)			
	7.5	11.0	13.0	15.0
Reynolds number (Re)	5.75×10^4	8.44×10^4	9.97×10^4	1.15×10^5
Mach number ($M = V_0/c$) (c=sound vel.)	0.023	0.033	0.039	0.045
Kinematic viscosity (v) (m^2/s)		1.3×10^{-4}		
Smagorinsky's constant (C_S)		0.12		
Characteristic dimension (L_0) (m)		1.0		

damping ratio and m the corresponding mass). Then, the structural damping is given by $C_S = 2m\xi^i\omega^i n$, where ω_n is the circular natural frequency and the superscript i indicates the corresponding mode.

The mean amplitudes in the X and Y directions (see Fig. 9) obtained for the downstream component of a twin cable arrangement are shown in Fig. 11. Wind velocities equal to 7.5, 11, 13 and 15 m/s were analyzed. It may be observed that numerical results are close to those obtained experimentally. In Fig. 11 it is shown that the critical velocity value computed numerically is smaller than the onset velocity obtained in a wind tunnel test. In other words, the galloping phenomenon, using the numerical algorithm presented here, is anticipated when compared to the

Table 4
Structural data according to the cables set arrangement

Structural properties	Cables set arrangement	
	Leeward cable of a twin set	Three bundled cables
Translational stiffness—(N/m)	1812.06	6779.23
Translational mass—(kg/m)	20.4	53.0
Natural frequency (f_n)—(Hz)	1.5	1.8
Scruton number ($Sc = 2m\delta/\rho D^2$)	57	40

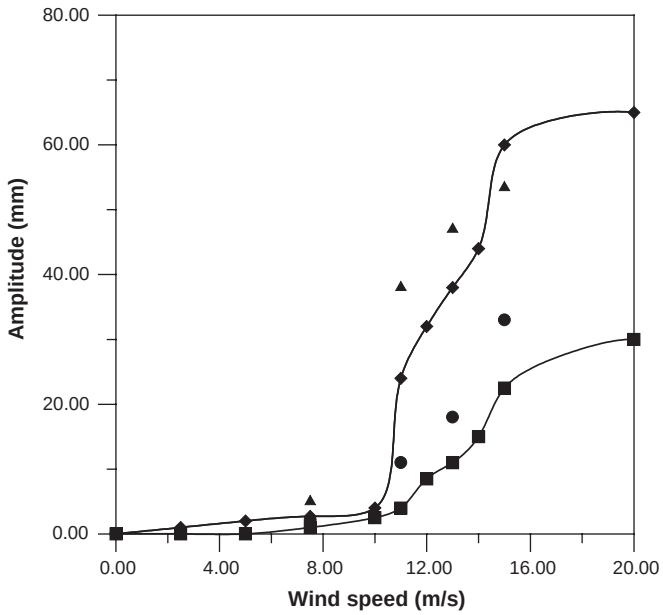

Fig. 11. Mean amplitudes as functions of the wind velocity for the downstream component of a twin cable arrangement. X direction: (●) present work; (■) Tokoro et al. [4]. Y direction: (▲) present work; (◆) Tokoro et al. [4].

experimental results. Furthermore, the mean amplitudes obtained in the X direction are a bit higher than the experimental analysis. It reveals a stronger coupled vibration for the numerical model.

The mean amplitudes in the Y direction (see Fig. 10) referred to the three bundled cables are presented in Fig. 12 for wind velocities equal to 9, 9.6 and 12 m/s. It can be observed that the critical velocity is located in an interval between 9 and 9.6 m/s. Nagao et al. [5] reported a higher value for the critical velocity, located in an interval ranging from 9.75 to 10.75 m/s. It can be seen that a reasonable agreement is obtained between the present work and the experimental model.

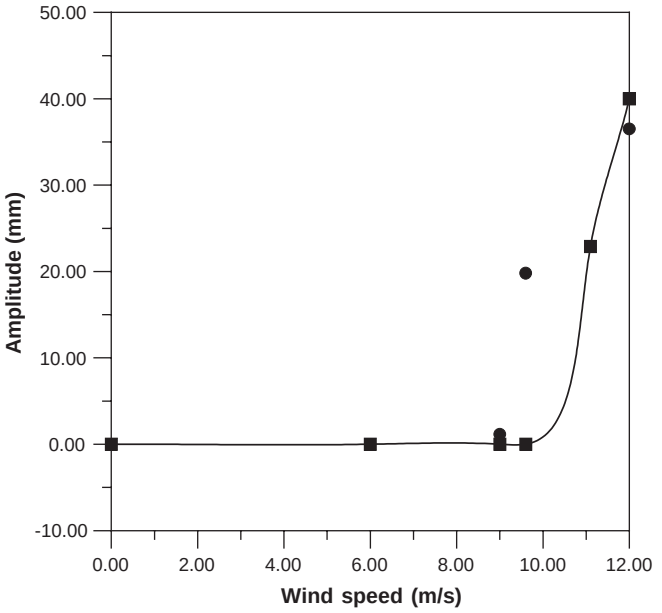

Fig. 12. Mean amplitudes in Y direction as functions of the wind velocity for three bundled cables: (●) present work; (■) Nagao et al. [5].

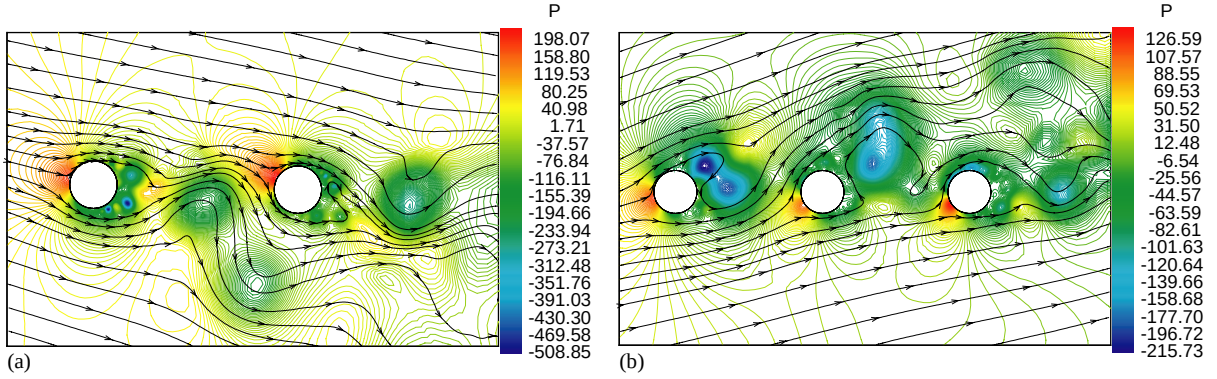

Fig. 13. Instantaneous streamlines and pressure fields obtained in the aeroelastic analysis: (a) wake galloping in a downstream component of a twin cable arrangement; and (b) galloping in three bundled cables.

Instantaneous pressure fields and streamlines are presented in Fig. 13. The wind velocities are 15 and 12 m/s, for the twin cable arrangement and the three bundled cables, respectively. It can be visualized that due to the proximity among the cylinders, bodies located downstream are greatly influenced by the wake of the bodies located upstream, principally for incidence angles ranging from 10° to 20°. This kind of dynamic instability is the well-known "*wake galloping*" phenomenon.

7. Conclusions

A numerical model to simulate wind action on bundled cables of electrical energy transmission lines was presented in this work. The computer code was able to get good results when compared to those obtained in wind tunnel tests by other authors for aerodynamic and aeroelastic problems. Important aerodynamic and aeroelastic aspects related to the analysis of cables were well demonstrated and some commentaries were included in Section 6; they will be briefly summarized below:

(1) Wake interference implications on the force coefficients, like drag reduction due to the transition anticipation for tandem arrangements and the increasing of the lift force as a function of the asymmetry of the cables with respect to the stream direction, were well reproduced
(2) Galloping and wake galloping characteristics, such as the suddenly growth of vibration amplitudes after the onset velocity is reached (which is a relative low velocity), were observed, according to previous experimental experiences. Furthermore, wind incidence angles used in the numerical simulations have proven to be in a critical range with respect to the dynamic instability phenomenon, as it was observed in experimental works presented here.

Some improvements may be still implemented on the computational code in order to obtain a more efficient numerical process:

(1) Sub-domains with different time intervals may be introduced using an algorithm employing sub cycles, similar to that presented by Teixeira and Awruch [28].
(2) Pressure may be determined with an implicit scheme using a Poisson equation; although more memory will be required, it will be possible to use larger time intervals, and probably spurious oscillations, which sometimes appear in the explicit scheme, will be eliminated.
(3) A dynamic sub-grid scale model for turbulence simulation with LES may be used; this model takes automatically a variable value for C_0 in the calculation of the eddy viscosity (see Murakami [16]).
(4) The displacements of the bundled cables produce axial stresses, introducing geometrically nonlinear effects, which may be considered using a geometrically nonlinear matrix.
(5) Perhaps the most important aspect would be the implementation of a 3-D model, substituting the sectional model presented in this work.

These improvements will be incorporated in future works, following an on-going research about CFD applications in *Computational Wind Engineering*.

References

[1] J.P. Den Hartog, *Mechanical Vibrations*, 4th ed., McGraw-Hill, New York, 1956.
[2] R.L. Wardlaw, K.R. Cooper, J.A. Watts, Wind tunnel and analytical investigations into the aeroelastic behaviour of bundled conductors, *IEEE Transactions on Power Apparatus and Systems V* PAS-94 (2) (1975) 642–654.

[3] S.J. Price, Wake induced flutter of power transmission conductors, *Journal of Sound and Vibration* 38 (1975) 125–147.
[4] S. Tokoro, H. Komatsu, M. Nakasu, K. Mizuguchi, A. Kasuga, A study on wake-galloping employing full aeroelastic twin cable model, *Journal of Wind Engineering and Industrial Aerodynamics* 88 (2000) 247–261.
[5] F. Nagao, H. Utsunomiya, M. Noda, M. Imoto, R. Sato, Aerodynamic properties of closely spaced triple circular cylinders, *Journal of Wind Engineering and Industrial Aerodynamics* 91 (2003) 75–82.
[6] R.L. Wardlaw, Interference and proximity effects, in: H. Sockel (Ed.), *Wind Excited Vibrations of Structures*, Springer, New York, 1994.
[7] T.T. Oliveira, Study of the Bundled Conductors Instability in Aerial Transmission Lines, MSc Thesis, Porto Alegre PPGEC/UFRGS, 2002 (in Portuguese).
[8] M.M. Alam, M. Moriya, K. Takai, H. Sakamoto, Fluctuating fluid forces on two circular cylinders in a tandem arrangement at a subcritical Reynolds number, *Journal of Wind Engineering and Industrial Aerodynamics* 91 (2003) 139–154.
[9] B. Tabarrok, J. Su, Semi-implicit Taylor–Galerkin finite element method for incompressible viscous flows, *Computer Methods in Applied Mechanics and Engineering* 117 (1994) 391–410.
[10] A.L. Rossa, A.M. Awruch, 3-D finite element analysis of incompressible flows with heat transfer, *Proceedings of the Second International Conference on Computational Heat and Mass Transfer*, COPPE/UFRJ, Rio de Janeiro, Brazil, October 2001, pp. 22–26.
[11] C.W. Hirt, A.A. Amsden, J.L. Cook, An arbitrary Lagrangean–Eulerian computing method for all flow speeds, *Journal of Computational Physics* 14 (1974) 227–253.
[12] T.J.R. Hughes, W.K. Liu, T.K. Zimmerman, Lagrangean Eulerian finite element formulation for incompressible viscous flows, *Computer Methods in Applied Mechanics and Engineering* 29 (1981) 329–349.
[13] J. Donea, S. Giuliani, J.P. Halleux, An arbitrary Lagrangean–Eulerian finite element method for transient dynamic fluid–structure interactions, *Computer Methods in Applied Mechanics and Engineering* 33 (1982) 689–723.
[14] W.K. Liu, H. Chang, T. Belytschko, Arbitrary Lagrangean Eulerian Petrov-Galerkin finite elements for nonlinear continua, *Computer Methods in Applied Mechanics and Engineering* 68 (1988) 259–310.
[15] D.J. Benson, An efficient accurate simple ALE method for nonlinear finite element programs, *Computer Methods in Applied Mechanics and Engineering* 72 (1989) 305–350.
[16] S. Murakami, Current status and future trends in computational wind engineering, *Journal of Wind and Industrial Aerodynamics* 67–68 (1997) 3–34.
[17] K.J. Bathe, *Finite Element Procedures*, Prentice Hall, Englewood Cliffs, NJ, 1996.
[18] H. Schlichting, *Boundary-Layer Theory*, 2nd ed., McGraw-Hill, New York, 1979.
[19] J. Sarrate, A. Huerta, J. Donea, Arbitrary Lagrangean–Eulerian formulation for fluid-rigid body interaction, *Computer Methods in Applied Mechanics and Engineering* 190 (2001) 3171–3188.
[20] A.J. Chorin, A numerical method for solving incompressible viscous flow problems, *Journal of Computational Physics* 2 (1967) 12–26.
[21] M. Kawahara, H. Hirano, A finite element method for high Reynolds number viscous fluid flow using two step explicit scheme, *International Journal for Numerical Methods in Fluids* 3 (1983) 137–163.
[22] J. He, C.C.S. Song, Evaluation of pedestrian winds in urban area by numerical approach, *Journal of Wind Engineering and Industrial Aerodynamics* 81 (1999) 295–309.
[23] J. Smagorinsky, General circulation experiments with the primitive Equations I, the basic experiment, *Monthly Weather Review* 91 (1963) 99–165.
[24] K.T. Yoon, S.Y. Moon, S.A. Garcia, G.W. Heard, T.J. Chung, Flow field-dependent mixed explicit-implicit (FDMEI) methods for high and low speed and compressible and incompressible flows, *Computer Methods in Applied Mechanics and Engineering* 151 (1998) 75–104.
[25] A.L. Braun, A.M. Awruch, Numerical simulation of the wind action on a long-span bridge deck, *Journal of the Brazilian Society of Mechanical Sciences and Engineering* 25 (4) (2003) 352–363.
[26] J.N. Reddy, D.K. Gartling, *The Finite Element Method in the Heat Transfer and Fluid Dynamics*, CRC Press, Boca Raton, FL, 1994.
[27] P.M. Gresho, R.L. Sani, *Incompressible Flow and the Finite Element Method, Advection-Diffusion and Isothermal Laminar Flow*, Wiley, Sussex, UK, 1999.

[28] P.R.F. Teixeira, A.M. Awruch, Three dimensional simulation of high compressible flows using a multi-time-step integration technique with subcycles, *Applied Mathematical Modeling* 25 (2001) 613–627.
[29] P.R.F. Teixeira, A.M. Awruch, Analysis of compressible fluids and elastic structures interaction by the finite element method, *Proceedings of the 16th Brazilian Congress of Mechanical Engineering*, COBEM 2001, Uberlândia (MG–Brazil), November 2001, pp. 45–54.
[30] R.L. Wardlaw, K.R. Cooper, Mechanism and alleviation of wind-induced structural vibrations, *Second Symposium on Applications of Solid Mechanics*, McMaster University, Hamilton, Canada, 1974, pp. 369–399.